Imaging Agents

DOI: 10.1002/anie.200802469

Multifunctional Uniform Nanoparticles Composed of a Magnetite Nanocrystal Core and a Mesoporous Silica Shell for Magnetic Resonance and Fluorescence Imaging and for Drug Delivery**

Jaeyun Kim, Hoe Suk Kim, Nohyun Lee, Taeho Kim, Hyoungsu Kim, Taekyung Yu, In Chan Song, Woo Kyung Moon, and Taeghwan Hyeon**

During the past two decades, extensive research has been carried out on the biomedical applications of nanostructured materials.[1] Among these various nanomaterials, mesoporous silica materials[2] have been intensively investigated for their potential application as delivery vehicles[3] for small-molecule drugs, DNA, and proteins, owing to their uniform pore size, large surface area, and high accessible pore volume. However, to date, there are only a few reports on the in vivo application of mesoporous silica materials administrated by intravenous injection,[4] because it is difficult to synthesize discrete and monodisperse mesoporous silica particles smaller than around 100 nm that possess high colloidal stability in a physiological environment and small enough size to allow a long blood circulation. In general, bigger nanoparticles (NPs) result in more rapid uptake by the reticuloendothelial system (RES), such as liver and spleen, but smaller NPs can escape from phagocytes in RES and circulate through blood vessels with a long blood half-life.[5] Although there have been several reports on the synthesis of uniform mesoporous silica particles smaller than 200 nm observed in TEM,[6] the particles are not discrete but aggregated. Consequently, it is still a challenge to synthesize discrete, monodisperse, and size-controllable mesoporous silica NPs for in vivo applications.

Recently, multifunctional nanostructured materials have been applied to multimodal imaging[7] and simultaneous diagnosis and therapy.[8] In this context, the integration of mesoporous silica with superparamagnetic monodisperse nanocrystals to form uniform core–shell composite particles has great potential for simultaneous bioimaging and drug delivery. Although there have been several reports on composite materials of magnetic nanocrystals and mesoporous silica materials,[9] these materials have not been used for in vivo applications because of their size and aggregation. Herein, we present discrete, monodisperse, and precisely size-controllable core–shell mesoporous silica NPs smaller than 100 nm by using single Fe_3O_4 nanocrystals as cores (designated as Fe_3O_4@mSiO_2). We also demonstrate the multifunctional bioapplications of the core–shell NPs for simultaneous magnetic resonance (MR) and fluorescence imaging, and for drug delivery.

The synthetic protocol is represented in Scheme 1. Cetyltrimethylammonium bromide (CTAB) serves not only as the stabilizing surfactant for the transfer of hydrophobic Fe_3O_4 nanocrystals[10] to the aqueous phase[11] but also as the organic template for the formation of mesopores in the sol–gel reaction.[2] After removing the CTAB templates from the as-synthesized materials by heating them at reflux in acidic ethanol solution (pH 1.4), we collected the Fe_3O_4@mSiO_2 particles. When we decreased the pH value of the extraction solution below 1.0, Fe_3O_4 nanocrystals as well as CTAB were fully removed from the as-synthesized Fe_3O_4@mSiO_2, resulting in hollow mesoporous silica NPs (designated as H-mSiO_2). Finally, for biomedical applications, the surface of the NPs was modified with PEG to render them biocompatible by

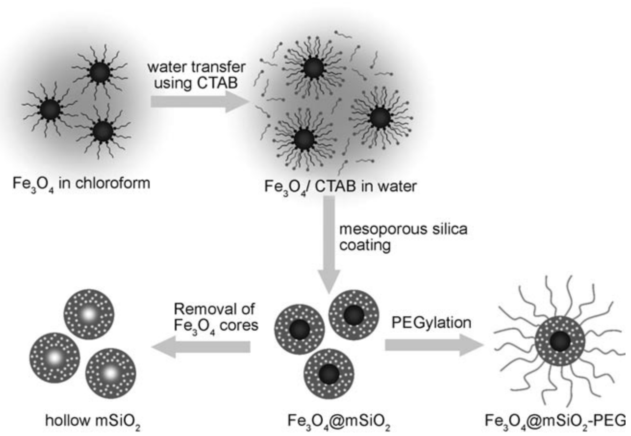

Scheme 1. Schematic illustration of the synthetic procedure for magnetite nanocrystal / mesoporous silica core–shell NPs.

---

[*] Dr. H. S. Kim,[+] H. Kim, Prof. I. C. Song, Prof. W. K. Moon
Diagnostic Radiology, Seoul National University Hospital and
the Institute of Radiation Medicine, Medical Research Center
Seoul National University, Seoul 110-744 (Korea)
Fax: (+82) 2-743-6385
E-mail: moonwk@radcom.snu.ac.kr

Dr. J. Kim,[+] N. Lee, T. Kim, Dr. T. Yu, Prof. T. Hyeon
National Creative Research Initiative Center for Oxide Nanocrystalline Materials and School of Chemical and Biological Engineering
Seoul National University, Seoul 151-744 (Korea)
Fax: (+82) 2-886-8457
E-mail: thyeon@snu.ac.kr

[+] These authors contributed equally to this work.

[**] T.H. acknowledges financial support by the Korean Ministry of Education, Science and Technology through the National Creative Research Initiative Program of the Korea Science and Engineering Foundation (KOSEF). This study was supported in part by a grant from the Innovative Research Institute for Cell Therapy, Republic of Korea (A062260).

Supporting information for this article is available on the WWW under http://dx.doi.org/10.1002/anie.200802469.

preventing the nonspecific adsorption of proteins to the NPs. The terminal succinimidyl end group of PEG was conjugated with the amine groups in the amine-modified Fe_3O_4@$mSiO_2$.

TEM reveals that 53 and 45 nm Fe_3O_4@$mSiO_2$ particles with 15 and 22 nm Fe_3O_4 core, respectively, are uniform and separated from one another (Figure 1 a–c and Figures S1, S2 in the Supporting Information). The colloidal packing observed in the TEM image (Figure 1 a) clearly demonstrates the uniformity of the NPs. The wormhole-like mesopores with diameters of around 2–3 nm were observed in the silica shells. The TEM image of H-$mSiO_2$ clearly shows the central hollow cores generated by the removal of the Fe_3O_4 nanocrystals (Figure 1 d–f and Figures S3, S4 in the Supporting Information). To date, there has been no report on the successful size control of uniform and discrete mesoporous silica NPs smaller than 100 nm. Using our current synthetic method, we were able to precisely control the size of the mesoporous silica NPs. We synthesized Fe_3O_4@$mSiO_2$ particles with diameters of 45, 60, 90, and 105 nm (Figure 1 g–j) simply by varying the concentration of the core nanocrystals during the formation of the mesoporous silica shell. As the concentration of the core nanocrystals decreased, the size of the resulting Fe_3O_4@$mSiO_2$ increased. The mesoporous silica shell can be coated on other nanocrystals with different compositions and shapes. For example, we successfully synthesized MnO@$mSiO_2$ using 25 nm MnO nanocrystals that have recently been used as a T_1 MRI contrast agent (Figure 1 k).[12] We were also able to coat mesoporous silica on one-dimensional nanostructures. For example, α-FeOOH nanotubes[13] were coated with a uniform mesoporous silica shell (Figure 1 l and Figures S5, S6 in the Supporting Information) using a very similar synthetic procedure to that employed for the spherical nanocrystals. Since most uniform and highly crystalline nanocrystals are synthesized by the thermal decomposition method[14] and are therefore hydrophobic, our simple and highly reproducible synthetic process can be a good protocol for the generalized fabrication of uniform nanocrystal core/mesoporous silica shell structures.

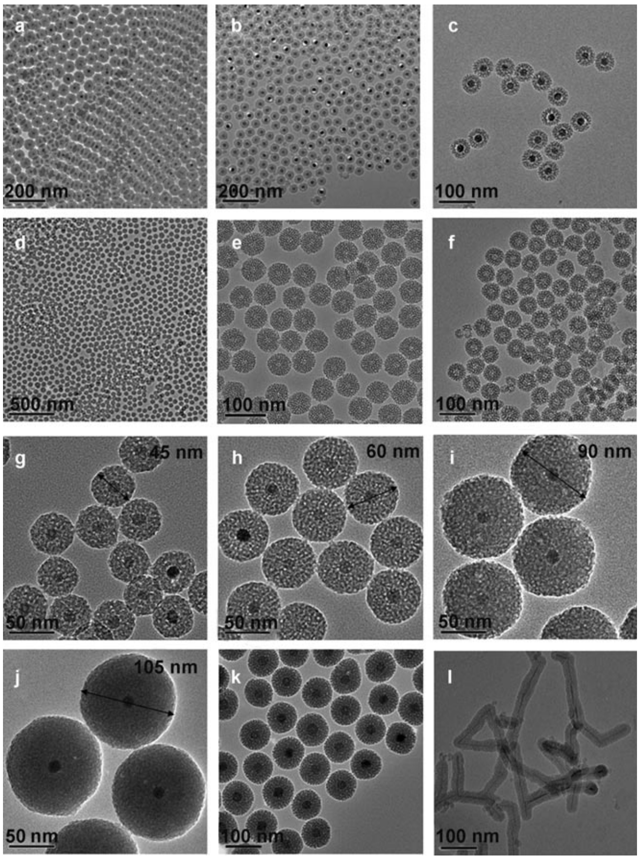

Figure 1. TEM images of core–shell and hollow mesoporous silica NPs. a) 53 nm Fe_3O_4@$mSiO_2$ with 15 nm core. b, c) 45 nm Fe_3O_4@$mSiO_2$ with 22 nm core. d, e) H-$mSiO_2$ from (a). f) H-$mSiO_2$ from (b, c). Different sized uniform 15 nm Fe_3O_4@$mSiO_2$ of g) 45 nm, h) 60 nm, i) 90 nm, and j) 105 nm. k) MnO@$mSiO_2$. l) α-FeOOH@$mSiO_2$. Large-magnification TEM images of each product are supplied in the Supporting Information.

Fe_3O_4@$mSiO_2$ has multiple functionalities applicable to simultaneous multimodal imaging and therapy. The field-dependent magnetism of Fe_3O_4@$mSiO_2$ particles at 300 K shows no hysteresis (Figure 2 a), demonstrating that they are superparamagnetic, which is a desirable characteristic for T_2 MR contrast agents.[15] The r_1 and r_2 relaxivity values of the Fe_3O_4@$mSiO_2$ with 15 nm Fe_3O_4 core were 3.40 and 245 $mM^{-1}s^{-1}$, respectively ($r_2/r_1 = 72.1$). N_2 adsorption/desorption isotherms (Figure 2 b) and the corresponding BJH pore size distribution (inset of Figure 2 b) demonstrate that Fe_3O_4@$mSiO_2$ has well-developed 2.6 nm mesopores; the BET surface area and the total pore volume were 481 and 1.07 $cm^3 g^{-1}$, respectively. For fluorescence imaging, fluorescein isothiocyanate (FITC) and rhodamine B isothiocyanate (RITC) were incorporated covalently into the silica walls by treating these dyes with 3-aminopropyltriethoxysilane and carrying out a subsequent silica sol–gel reaction. The dye-derivatized NPs (Fe_3O_4@$mSiO_2$(F) and Fe_3O_4@$mSiO_2$(R)) dispersed in water showed the typical emissions of fluorescein and rhodamine B at 516 and 577 nm, respectively (Figure 2 c).

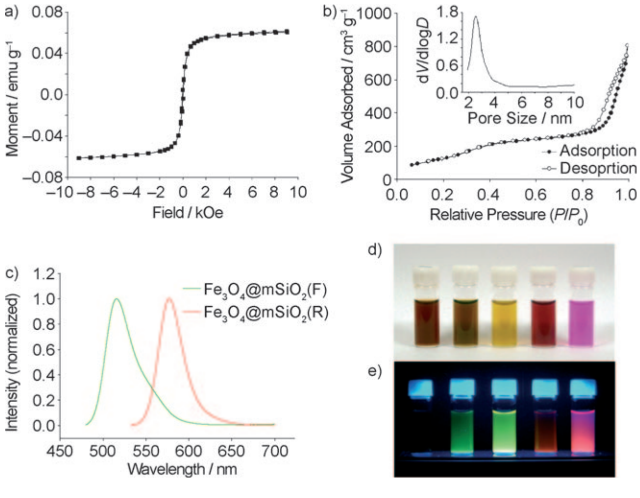

Figure 2. Characterization of Fe_3O_4@$mSiO_2$. a) Field-dependent magnetization at 300 K. b) N_2 adsorption/desorption isotherms (inset: pore size distribution from adsorption branch; V = pore volume, D = pore size). c) Photoluminescence spectra of Fe_3O_4@$mSiO_2$(F) ($\lambda_{ex} = 460$ nm) and Fe_3O_4@$mSiO_2$(R) ($\lambda_{ex} = 520$ nm). d, e) Dispersion of Fe_3O_4@$mSiO_2$ without dye functionalization, Fe_3O_4@$mSiO_2$(F), H-$mSiO_2$(F), Fe_3O_4@$mSiO_2$(R), and H-$mSiO_2$(R) (left to right) in water under white light (d) and UV light (e).

All NPs of the $Fe_3O_4@mSiO_2$ without the dye, the dye-anchored $Fe_3O_4@mSiO_2$, and the dye-anchored H-$mSiO_2$ were well-dispersible in water (Figure 2d). Under UV excitation, the dye-doped mesoporous silica NPs emitted different colors depending on the incorporated dyes, while there was no fluorescence from the $Fe_3O_4@mSiO_2$ without the dye (Figure 2e). The H-$mSiO_2$ exhibited brighter fluorescence than the $Fe_3O_4@mSiO_2$ owing to the absence of Fe_3O_4 nanocrystals, which partially quench the fluorescence of the dye. Derivatization with PEG increased the colloidal stability of the NPs in phosphate-buffered saline (PBS) solution. Dynamic light scattering (DLS) measurements revealed that the hydrodynamic size of $Fe_3O_4@mSiO_2$(R)-PEG in PBS solution is approximately 97 nm (Figure S7 in the Supporting Information), demonstrating that no aggregation occurred.

Cell viability by the MTT assay (MTT = 3-(4,5-dimethylthiazol-2-yl)-2,5-diphenyltetrazolium bromide) and proliferative activity by trypan blue exclusion assays (Figure S8 in the Supporting Information) revealed that the cell viability and proliferation were not hindered by the presence of the $Fe_3O_4@mSiO_2$(R)-PEG up to a concentration of $10\ \mu g\,Fe\,mL^{-1}$ (equal to $350\ \mu g\,mL^{-1}$ $Fe_3O_4@mSiO_2$(R)-PEG). TC_{50} of the $Fe_3O_4@mSiO_2$(R)-PEG under incubation for 6 h was $67.5 \pm 2.7\ \mu g\,Fe\,mL^{-1}$ (Figure S9 in the Supporting Information). We explored the cellular uptake of the $Fe_3O_4@mSiO_2$(R)-PEG by incubating MCF-7 breast cancer cells with different concentrations of NPs in serum-containing media for various incubation times. The fluorescence microscopy and confocal laser scanning microscopy (CLSM) images reveal that the uptake of $Fe_3O_4@mSiO_2$(R)-PEG was dose- and time-dependent (Figure S10 in the Supporting Information). The NPs were spontaneously internalized into MCF-7 cells by endocytosis, and their uptake was clearly observed within 30 min. The CLSM image of the MCF-7 cells incubated with $2.5\ \mu g\,Fe\,mL^{-1}$ of the NPs for 1 h showed that the internalized red-emitting $Fe_3O_4@mSiO_2$(R)-PEG was found in the cytoplasm of the MCF-7 cells, but not in the nucleus (Figure S11a in the Supporting Information). The TEM image of the cells also provides direct evidence that a large number of the NPs were endocytosed into the MCF-7 cells and that the core–shell nanostructures were maintained after endocytosis (Figure S11b in the Supporting Information). We checked the in vitro multimodal imaging and drug loading capability of the NPs. The fluorescent and T_2-weighted MR images (Figure S11c,d in the Supporting Information) of phantoms showed that as the concentration of the NPs was increased, a brighter fluorescence of rhodamine B and a darker T_2 signal were observed. To examine the drug delivery of the NPs, the cytotoxic effect of doxorubicin (DOX)-loaded $Fe_3O_4@mSiO_2$(R)-PEG was tested on SK-BR-3 cells (Figure S12 in the Supporting Information). The cytotoxic efficacy of the DOX-loaded $Fe_3O_4@mSiO_2$(R)-PEG increased as the concentration of DOX-loaded NPs was increased, while $Fe_3O_4@mSiO_2$(R)-PEG alone did not show cytotoxicity to cancer cells even at high concentration. This result indicates that $Fe_3O_4@mSiO_2$ has a potential for drug loading and delivery into cancer cells to induce cell death.

In preliminary in vivo animal experiments, we subcutaneously injected MCF-7 cells labeled with $Fe_3O_4@mSiO_2$(R)-PEG ($10\ \mu g\,Fe\,mL^{-1}$) and control MCF-7 cells without labeling into each dorsal shoulder of a nude mouse. The labeled MCF-7 cells were clearly detectable as a dark volume of subcutaneous tumor in the T_2-weighted image (Figure 3a) and as a strong red fluorescence through an RITC filter (Figure 3b), while the unlabeled MCF-7 cells showed insignificant effects on both.

Then we investigated the potential for in vivo imaging of $Fe_3O_4@mSiO_2$(R)-PEG by tracking the particles' passive tumor accumulation. It is known that when NPs with high colloidal stability under physiological conditions and size smaller than around 200 nm are injected intravenously, parts of NPs accumulate preferentially at tumor sites through their enhanced permeability and retention (EPR) effect in passive targeting.[16] We intravenously injected the NPs into the nude mice ($n = 2$) bearing tumors with diameter of 0.5 cm on their shoulder and obtained T_2-weighted MR images before injection, and 2 h and 24 h after injection (Figure 3c). At

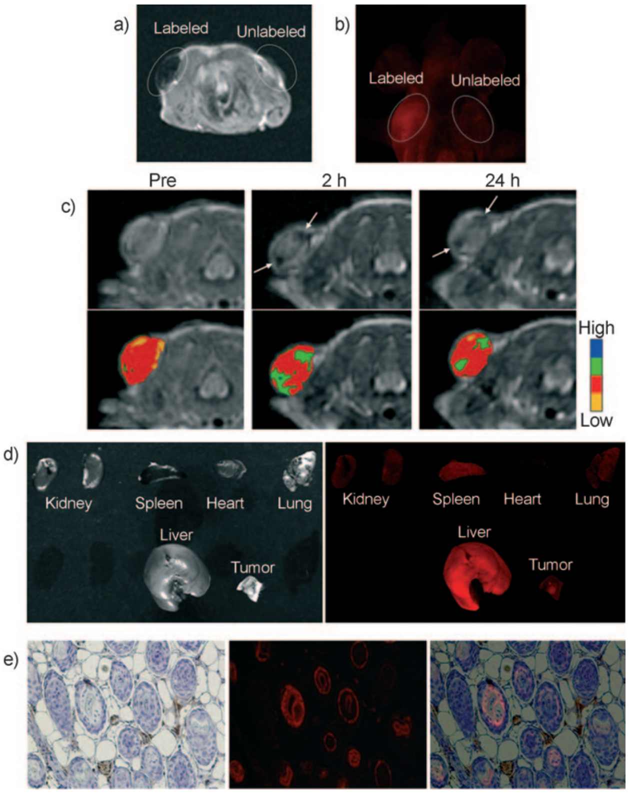

Figure 3. In vivo multimodal imaging using $Fe_3O_4@mSiO_2$. a) In vivo T_2-weighted MR and b) fluorescence images of subcutaneously injected MCF-7 cells labeled with $Fe_3O_4@mSiO_2$(R) ($10\ \mu g\ Fe\,mL^{-1}$) and control MCF-7 cells without labeling into each dorsal shoulder of a nude mouse. c) In vivo T_2-weighted MR images (upper row) and color maps (lower row) of T_2-weighted MR images of tumor before and after the $Fe_3O_4@mSiO_2$(R) ($5\ mg\ Fe\,kg^{-1}$) was intravenously injected into the tail vein of a nude mouse implanted with MCF-7 cells. A decrease of signal intensity on T_2-weighted MR images was detected at the tumor site (arrows). d) Photographic image and corresponding fluorescence image of several organs and the xenograft tumor 24 h after intravenous injection. e) Immunostaining of vasculature (brown) with anti-CD31 antibody and counterstaining of nucleus with hematocylin (blue; left), a fluorescence image of the $Fe_3O_4@mSiO_2$(R) (middle), and a merged image (right) in sectioned tumor. The images and paraffin section of tumor were taken after sacrifice 24 h after injection of the NPs.

2 h after the injection, the accumulation of the NPs in tumors could be detected in the T_2-weighted MR images. Even at 24 h after injection the NPs still remained in tumor sites. To confirm the accumulation of $\mathrm{Fe_3O_4@mSiO_2(R)}$-PEG into the tumor site, the mice were sacrificed 24 h after the injection and several organs were investigated using a fluorescence imaging system (Figure 3 d). The strong fluorescence from the tumor was observed, representing the appreciable accumulation of the NPs in tumors through the EPR effect. The accumulation in the rest of the organs, including liver and kidney, showed the typical accumulation, consistent with previous reports on intravenous administration of iron oxide NPs with dextran coating.[8e]

To verify the existence of $\mathrm{Fe_3O_4@mSiO_2(R)}$ in tumor tissue, the tumor tissue in Figure 3 d was sectioned and observed under fluorescence microscopy (Figure 3 e). We performed immunostaining for CD31, which is expressed constitutively on the surface of endothelial cells and is weakly expressed on many peripheral leukocytes and platelets. CD31-positive vasculatures were found in tumors, indicating that the vasculature of tumor tissues were developed (brown colors, left image in Figure 3 e). The nuclei were stained blue with hematocylin. The accumulated $\mathrm{Fe_3O_4@mSiO_2(R)}$-PEG in tumor cells were observed by RITC filter (middle image in Figure 3 e). To the best of our knowledge, this is the first report on the accumulation of intravenously injected mesoporous silica NPs in a tumor site. $\mathrm{Fe_3O_4@mSiO_2(R)}$-PEG particles are stable under physiological conditions and circulate for a long enough time to accumulate in the tumor sites through the EPR effect. In terms of their in vivo biocompatibility, we observed no distinct toxicity in the nude mice administered with $\mathrm{Fe_3O_4@mSiO_2(R)}$-PEG over the monitoring period.

In conclusion, we synthesized discrete and monodisperse mesoporous silica NPs consisting of a single Fe_3O_4 nanocrystal core and a mesoporous silica shell. The size of the mesoporous silica NPs can be easily controlled below 100 nm. The current synthetic protocol can be generalized to produce core–shell NPs composed of a single hydrophobic nanocrystal core and mesoporous silica shell. The integrated capability of the core–shell NPs to be used as MR and fluorescence imaging agents, along with their potential use as a drug delivery vehicle, make them a novel candidate for future cancer diagnosis and therapy.

Received: May 27, 2008
Revised: July 17, 2008

Keywords: drug delivery · fluorescence · magnetic resonance · mesoporous materials · nanostructures

---

[1] a) D. Peer, J. M. Karp, S. Hong, O. C. Farokhzad, R. Margalit, R. Langer, *Nat. Nanotechnol.* **2007**, *2*, 751; b) V. P. Torchilin, *Nat. Rev. Drug Discovery* **2005**, *4*, 145; c) R. Duncan, *Nat. Rev. Cancer* **2006**, *6*, 688; d) X. Gao, Y. Cui, R. M. Levenson, L. W. K. Chung, S. Nie, *Nat. Biotechnol.* **2004**, *22*, 969.

[2] C. T. Kresge, M. E. Leonowicz, W. J. Roth, J. C. Vartuli, J. S. Beck, *Nature* **1992**, *359*, 710.

[3] I. I. Slowing, B. G. Trewyn, S. Giri, V. S.-Y. Lin, *Adv. Funct. Mater.* **2007**, *17*, 1225.

[4] K. M. K. Taylor, J. S. Kim, W. J. Rieter, H. An, W. Lin, W. Lin, *J. Am. Chem. Soc.* **2008**, *130*, 2154.

[5] D. C. Drummod, O. Meyer, K. Hong, D. B. Kirpotin, D. Papahadjopoulos, *Pharmacol. Rev.* **1999**, *51*, 691.

[6] a) C. E. Fowler, D. Khushalani, B. Lebeau, S. Mann, *Adv. Mater.* **2001**, *13*, 649; b) S. Huh, J. W. Wiench, J.-C. Yoo, M. Pruski, V. S.-Y. Lin, *Chem. Mater.* **2003**, *15*, 4247; c) K. Suzuki, K. Ikari, H. Imai, *J. Am. Chem. Soc.* **2004**, *126*, 462.

[7] a) J.-H. Lee, Y.-w. Jun, S.-I. Yeon, J.-S Shin, J. Cheon, *Angew. Chem.* **2006**, *118*, 8340; *Angew. Chem. Int. Ed.* **2006**, *45*, 8160; b) S. T. Selvan, P. K. Patra, C. Y. Ang, J. Y. Ying, *Angew. Chem.* **2007**, *119*, 2500; *Angew. Chem. Int. Ed.* **2007**, *46*, 2448; c) W. J. Rieter, J. S. Kim, K. M. L. Taylor, H. An, W. Lin, T. Tarrant, W. Lin, *Angew. Chem.* **2007**, *119*, 3754; *Angew. Chem. Int. Ed.* **2007**, *46*, 3680; d) C. Xu, J. Xie, D. Ho, C. Wang, N. Kohler, G. Walsh, J. R. Morgan, Y. E. Chin, S. Sun, *Angew. Chem.* **2008**, *120*, 179; *Angew. Chem. Int. Ed.* **2008**, *47*, 173.

[8] a) X. Huang, I. H. El-Sayed, W. Qian, M. A. El-Sayed, *J. Am. Chem. Soc.* **2006**, *128*, 2115; b) J. Kim, S. Park, J. E. Lee, S. M. Jin, J. H. Lee, I. S. Lee, I. Yang, J.-S. Kim, S. K. Kim, M.-H. Cho, T. Hyeon, *Angew. Chem.* **2006**, *118*, 7918; *Angew. Chem. Int. Ed.* **2006**, *45*, 7754; c) N. Nasongkla, E. Bey, J. Ren, H. Ai, C. Khemtong, J. S. Guthi, S.-F. Chin, A. D. Sherry, D. A. Boothman, J. Gao, *Nano Lett.* **2006**, *6*, 2427; d) W. S. Seo, J. H. Lee, X. Sun, Y. Suzuki, D. Mann, Z. Liu, M. Terashima, P. C. Yang, M. V. McConnell, D. G. Nishimura, H. Dai, *Nat. Mater.* **2006**, *5*, 971; e) Z. Medarova, W. Pham, C. Farrar, V. Petkova, A. Moore, *Nat. Med.* **2007**, *13*, 372.

[9] a) S. Giri, B. G. Trewyn, M. P. Stellmaker, V. S.-Y. Lin, *Angew. Chem.* **2005**, *117*, 5166; *Angew. Chem. Int. Ed.* **2005**, *44*, 5038; b) W. Zhao, J. Gu, L. Zhang, H. Chen, J. Shi, *J. Am. Chem. Soc.* **2005**, *127*, 8916; c) J. Kim, J. E. Lee, J. Lee, J. H. Yu, B. C. An, K. Kim, Y. Hwang, C. H. Shin, J. G. Park, J. Kim, T. Hyeon, *J. Am. Chem. Soc.* **2006**, *128*, 688; d) Y.-S. Lin, S.-H. Wu, Y. Hung, Y.-H. Chou, C. Chang, M.-L. Lin, C.-P. Tsai, C.-Y. Mou, *Chem. Mater.* **2006**, *18*, 5170; e) Y. Deng, D. Qi, C. Deng, X. Zhang, D. Zhao, *J. Am. Chem. Soc.* **2008**, *130*, 28; f) I. Gorelikov, N. Matsuura, *Nano Lett.* **2008**, *8*, 369.

[10] J. Park, K. An, Y. Hwang, J. G. Park, H. J. Noh, J. Y. Kim, J. H. Park, N. M. Hwang, T. Hyeon, *Nat. Mater.* **2004**, *3*, 891.

[11] a) H. Fan, K. Yang, D. M. Boye, T. Sigmon, K. J. Malloy, H. Xu, G. P. López, C. J. Brinker, *Science* **2004**, *304*, 567; b) H. Fan, A. Wright, J. Gabaldon, A. Rodriguez, C. J. Brinker, Y.-B. Jiang, *Adv. Funct. Mater.* **2006**, *16*, 891.

[12] H. B. Na, J. H. Lee, K. An, Y. I. Park, M. Park, I. S. Lee, D.-H. Nam, S. T. Kim, S. H. Kim, S.-W. Kim, K.-H. Lim, K.-S. Kim, S.-O. Kim, T. Hyeon, *Angew. Chem.* **2007**, *119*, 5493; *Angew. Chem. Int. Ed.* **2007**, *46*, 5397.

[13] T. Yu, J. Park, J. Moon, K. An, Y. Piao, T. Hyeon, *J. Am. Chem. Soc.* **2007**, *129*, 14558.

[14] J. Park, J. Joo, S. G. Kwon, Y. Jang, T. Hyeon, *Angew. Chem.* **2007**, *119*, 4714; *Angew. Chem. Int. Ed.* **2007**, *46*, 4630.

[15] J. W. Bulte, D. L. Kraitchman, *NMR Biomed.* **2004**, *17*, 484.

[16] I. Brigger, C. Dubernet, P. Couveur, *Adv. Drug Delivery Rev.* **2002**, *54*, 631.